REPORT

Crystallographic and chemical signatures in coral skeletal aragonite

Gabriela A. Farfan[1,2,3] · Amy Apprill[3] · Anne Cohen[4] · Thomas M. DeCarlo[5,6] ·
Jeffrey E. Post[1] · Rhian G. Waller[7] · Colleen M. Hansel[3]

Abstract Corals nucleate and grow aragonite crystals, organizing them into intricate skeletal structures that ultimately build the world's coral reefs. Crystallography and chemistry have profound influence on the material properties of these skeletal building blocks, yet gaps remain in our knowledge about coral aragonite on the atomic scale. Across a broad diversity of shallow-water and deep-sea scleractinian corals from vastly different environments, coral aragonites are remarkably similar to one another, confirming that corals exert control on the carbonate chemistry of the calcifying space relative to the surrounding seawater. Nuances in coral aragonite structures relate most closely to trace element chemistry and aragonite saturation state, suggesting the primary controls on aragonite structure are ionic strength and trace element chemistry, with growth rate playing a secondary role. We also show how coral aragonites are crystallographically indistinguishable from synthetic abiogenic aragonite analogs precipitated from seawater under conditions mimicking coral calcifying fluid. In contrast, coral aragonites are distinct from geologically formed aragonites, a synthetic aragonite precipitated from a freshwater solution, and mollusk aragonites. Crystallographic signatures have future applications in understanding the material properties of coral aragonite and predicting the persistence of coral reefs in a rapidly changing ocean.

Topic Editor Lauren T. Toth

✉ Gabriela A. Farfan
farfang@si.edu

✉ Colleen M. Hansel
chansel@whoi.edu

[1] Department of Mineral Sciences, National Museum of Natural History, Smithsonian Institution, Washington, DC, USA

[2] MIT-WHOI Joint Program in Oceanography/Applied Ocean Science and Engineering, Woods Hole Oceanographic Institution, Woods Hole, MA, USA

[3] Department of Marine Chemistry and Geochemistry, Woods Hole Oceanographic Institution, Woods Hole, MA, USA

[4] Department of Marine Geology and Geophysics, Woods Hole Oceanographic Institution, Woods Hole, MA, USA

[5] School of Earth Sciences, Oceans Institute, The University of Western Australia, Crawley, WA, Australia

[6] College of Natural and Computational Science, Hawai'i Pacific University, Honolulu, HI, USA

[7] Darling Marine Center, The University of Maine, Walpole, ME, USA

Introduction

Scleractinian coral skeletons form the framework of coral reef ecosystems, supporting a diversity of marine organisms, the livelihoods of hundreds of millions of people, and amassing an economic value of almost one trillion dollars (Carpenter et al. 2008; Hoegh-Guldberg et al. 2017). Ocean conditions are changing rapidly as carbon dioxide emissions accumulate, leading to mounting concerns that these changes will have devastating impacts on coral reefs, with some studies even predicting local extinctions of these valuable ecosystems by mid-century (Carpenter et al. 2008). Scleractinian corals (henceforth referred to simply as "corals") build their skeletons out of the mineral aragonite, a polymorph of calcium carbonate, which renders

them vulnerable to ocean acidification and shifts in ocean carbonate chemistry. Corals precipitate skeletons by manipulating seawater chemistry in an extracellular space between the base of the polyp and the top of the existing skeleton (Cohen and McConnaughey 2003; Tambutté et al. 2011). This calcifying fluid has been measured in terms of internal pH and internal aragonite saturation state (Ω_{cf}), using crystal morphology (Cohen et al. 2009; Holcomb et al. 2009), pH-sensitive dyes (Venn et al. 2011), microsensors (Cai et al 2016; Sevilgen et al 2019), boron isotopes (Allison et al. 2010; McCulloch et al. 2012a, b), and Raman spectroscopy (DeCarlo et al. 2017). These measurements all indicate that corals elevate aragonite saturation conditions well above that of surrounding sea-water. Several lines of evidence support that corals precipitate their skeletons from modified seawater: (1) spherules of synthetic aragonites precipitated from seawater exhibit the same acicular crystal bundle habits (crystal morphology) observed in coral skeletons (Cohen and McConnaughey 2003; Cohen et al. 2009; Holcomb et al. 2009), (2) the crystal habit response of coral aragonite to ocean acidification conditions mirrors that of synthetic aragonites, with juvenile corals reared under low saturation conditions precipitating blocky crystal habits that mimic synthetic aragonites formed from lower aragonite saturation states (Cohen et al. 2009), (3) coral aragonite geochemistry matches that of synthetic aragonites precipitated from seawater (Gaetani and Cohen 2006; Cohen and Gaetani 2010), and (4) aragonite carbonate bonding environments, as measured by Raman spectroscopy, are the same for corals and synthetic aragonites precipitated from seawater (DeCarlo et al. 2018). Beyond modifying the local saturation state conditions, corals produce organic molecules that appear to contribute to aragonite nucleation and growth. Specifically, organic molecules have also been found in coral skeletons (< 1 weight % of the skeleton, Cohen and McConnaughey 2003; Meibom et al. 2008; Benzerara et al. 2011), providing spatial evidence of their role in skeletal precipitation via actively templating and inducing aragonite formation lowering the Gibbs free energy barrier via heterogeneous nucleation (Levi et al. 1998; Cuif and Dauphin 2005; Mass et al. 2013; De Yoreo et al. 2015; Von Euw et al. 2017). Ultimately, coral skeletal health under climate change is dependent on the corals' ability to control their calcifying fluid chemistry and biomolecular templates.

The purpose of this study is to interrogate whether the end-products of coral calcification (the aragonite crystallites) produce crystallographic signatures that may indicate aragonite formation conditions and environmental stressors. In previous studies, crystal habits and crystallite orientation of coral aragonites have been shown to shift under stressful growth conditions, as determined by high-resolution scanning electron microscopy (SEM, Cohen et al. 2009; Hennige et al. 2015; Foster et al. 2016; Farfan et al. 2018), transmission electron microscopy (TEM, Benzerara et al. 2011; Van de Locht et al. 2013), and electron backscattered secondary electron diffraction (EBSD, Coronado et al. 2019). However, differences in mineral habits do not necessarily translate into differences in crystal structure and chemistry, which largely determine the material properties of a mineral (solubility, strength) and can have dramatic effects on how a mineral responds to the environment (Bischoff et al. 1985). Thus, an evaluation of preserved crystallographic signatures in aragonite produced via different (a)biotic processes may offer insights into the sensitivity of coral aragonite formation and skeletal stability under environmental changes.

Previous crystallographic studies of biogenic aragonites from mollusks (Pokroy et al. 2004, 2007; Antao 2012; Rao et al. 2016) and some corals (Stolarski et al. 2007; Coronado et al. 2019) determined that biogenic aragonites have distorted unit-cell axes compared to geological (natural, abiotic) aragonites (Dickens and Bowen 1971; Caspi et al. 2005), which have been attributed to the incorporation of biological molecules. Only recently have studies begun to combine crystallographic data with other geochemical and mineralogical measurements to suggest that substitutions of magnesium (Mg^{2+}) for calcium (Ca^{2+}) in the aragonite structure may be responsible for observed crystalline distortions in bivalves (Roger et al. 2017). More recent crystallographic investigations have also revealed shifts in coral aragonite mineralogy in response to ocean acidification conditions (Farfan et al. 2018; Coronado et al. 2019).

In the present study, we compare the crystallographic properties of aragonites formed by a diversity of corals spanning the shallow to deep sea and encompassing a range of growth rates and surrounding chemical environments. We then compare those coral aragonites to those formed by other organisms and abiotic processes. This comparison provides diagnostic crystallographic signatures of aragonite source and may offer further insight into controls on coral aragonite crystal formation. We also couple powder X-ray diffraction data and Rietveld refinement methods with Raman-based information about carbonate bonding environments and trace element incorporations to investigate controls on aragonite structural disorder. This multivariable dataset allows for a robust investigation into the parameters relating to crystallographic differences.

Materials and methods

Samples

Deep-sea corals

Samples of deep-sea azooxanthellate corals (DSACs), or "cold-water" corals, represent a range of DSAC species, skeletal architectures, and reef localities that were treated with bleach to remove organics and are described by Farfan et al. (2018) and references therein.

Shallow-water corals

In order to represent the range of possible growth environments in shallow-water tropical zooxanthellate corals (STZCs), we sampled STZCs from different locations with different local seawater chemistry and species that represent an array of skeletal habits (massive, branching). Corals and sampling sites included: *Pocillopora verrocusa* (Vavvaru, Maldives, 5°25.0923 N, 73°21.07326 E; 5 m), *Stylopora pistillata* (Nigaloo, Australia, 21°54.908 S, 113°57.424 E and 23°10.531 S, 113°45.552 E; 1.5–4.5 m), *Orbicella faveolata* (Gulf of Batabano, Cuba, 21°35.468 N, 81°55.675 W, 21°36.121 N, 81°56.060 W and 21°35.0772 N, 81°35.832; 4–10 m), *Montastrea cavernosa* (Gulf of Batabano, Cuba, 21°35.2158 N, 81°34.9848 W; 3–13 m), *Acropora palmata* (Gulf of Batabano, Cuba, 21°36.76116 N, 81°36.86952 W; 3–4.5 m), and *Acropora cervicornis* (Jardines de la Reina, Cuba, 20°52.65894, 78°58.21704; 1.5 m). Three distinct colonies were sampled for each shallow-coral species. One sample from each of the species was treated with bleach to remove organics (Farfan et al. 2018), while the others were powdered and left untreated. All STZCs and DSACs samples were subsampled from the coral septa, or as close to the septa as possible, so that samples contained the newest skeletal growth and to assure consistency across coral aragonite samples (additional information in Supplementary Materials, Extended Materials and Methods).

Other biogenic aragonites

We used a commonly utilized reference biogenic aragonite, JCp-1 *Porites* sp. coral from Japan (Okai et al. 2002) in both untreated and bleach-treated forms. It is important to note that the JCp-1 geochemical standard is a bulk standard, making it different from the fresh samples in this study that were sub-sampled from the newest growth along the septa.

In order to compare our coral crystallography to other biomineralized aragonites, we have included two untreated mollusk nacre samples from marine environments (likely estuarine) in Japan (Akoya pearl) and the Sea of Cortez, Baja California, Mexico, as well as a pearl sample from an unknown locality (MGMH-99527) in both untreated and bleach-treated forms.

Synthetic aragonites

As a comparison to coral and other naturally formed aragonites, we have included a suite of synthetic aragonites (f06, g04, g09, and h01) precipitated abiogenically from aragonite-supersaturated seawater held over a wide range of controlled aragonite saturation states and pHs. These synthetic aragonites were precipitated at 25 °C from $NaHCO_3$ and Na_2CO_3 solutions. Samples were precipitated from natural, 0.2 μm filtered Vineyard Sound (MA, the USA) seawater at Woods Hole Oceanographic Institution and are described in detail in DeCarlo et al. (2015) and Holcomb et al. (2016) and were previously measured crystallographically (Farfan et al. 2018). Additional samples g13 and h09 precipitated at lower aragonite saturation states (Ω_{Arg}) consistent with coral calcifying fluid aragonite saturation state (Ω_{cf}) were measured with Raman spectroscopy.

In contrast to synthetic aragonites precipitated from seawater, we have also included a synthetic aragonite formed from freshwater conditions by deionized water supersaturated with respect to aragonite. This synthetic aragonite sample is the result of a nine-month crystallographic transformation to aragonite from an unstable amorphous calcium carbonate (ACC) precursor phase which was created with 25.41% Mg at the Virginia Polytechnic Institute in a procedure described in Blue et al. (2017).

Geological aragonites

Natural aragonite samples, presumably formed by geological processes, were acquired from the Mineralogical and Geological Museum, Harvard University and the Virginia Tech Geosciences Museum collections and were collected from various localities around the globe (Table 1; Supplementary Table 1). We assume that all aragonites labeled as "geologically-formed" are formed via geological processes without any substantial biological influence. Additional information available in the Supplementary Materials, Extended Materials and Methods.

Table 1 Mean unit-cell parameters (± S.D.) and ranges for aragonites formed by different means (coral, synthetic, etc.) in this study, as well as in previous studies

This study, mean ± s.d	a-axis length (Å)	b-axis length (Å)	c-axis length (Å)	Volume (Å³)
Deep-sea corals (n = 32)	4.9664 ± 0.0015	7.9719 ± 0.0017	5.7529 ± 0.0018	227.76 ± 0.18
Ranges	4.9608–4.9683	7.9689–7.9769	5.7463–5.7564	227.16–228.14
shallow-water corals (n = 20)	4.9653 ± 0.0006	7.9731 ± 0.0018	5.752 ± 0.001	227.71 ± 0.09
Ranges	4.9638–4.9673	7.9707–7.9785	5.7501–5.7549	227.52–227.97
all corals (n = 112)	4.9658 ± 0.0011	7.9728 ± 0.0017	5.7527 ± 0.0013	227.75 ± 0.12
Ranges	4.9608–4.9683	7.9689–7.9785	5.7464–5.7564	227.16–228.14
JCp-1 reference coral (n = 8)	4.9649 ± 0.0005	7.9765 ± 0.0012	5.751 ± 0.0006	227.75 ± 0.08
Ranges	4.9644–4.9657	7.9754–7.9785	5.7501–5.7523	227.66–227.89
mollusk nacre (n = 16)	4.9629 ± 0.0027	7.9659 ± 0.0025	5.75 ± 0.002	227.32 ± 0.15
Ranges	4.9583–4.9660	7.9619–7.9702	5.7475–5.7563	227.02–227.67
Seawater synthetic aragonites (n = 16)	4.9649 ± 0.0006	7.9747 ± 0.0022	5.7526 ± 0.0008	227.76 ± 0.08
Ranges	4.9635–4.9659	7.9705–7.9778	5.7514–5.7538	227.61–227.87
Freshwater synthetic aragonites (n = 4)	4.9618 ± 0.0003	7.969 ± 0.0006	5.7477 ± 0.0003	227.26 ± 0.03
Ranges	4.9616–4.9621	7.9681–7.9698	5.7473–5.7482	227.21–227.29
Geological aragonites (n = 16)	4.962 ± 0.001	7.9694 ± 0.0023	5.7438 ± 0.0014	227.13 ± 0.15
Ranges	4.9603–4.9634	7.9655–7.9735	5.7416–5.7461	226.85–227.38
Previous studies, mean ± s.d	**a-axis length (Å)**	**b-axis length (Å)**	**c-axis length (Å)**	**Volume (Å³)**
Coral aragonite studies (n = 2)	4.96504 ± 0.00005	7.9711 ± 0.0012	5.7495 ± 0.0006	227.55 ± 0.06
Ranges	4.965–4.9651	7.9699–7.9723	5.7489–5.75	227.49–227.60
Mollusk aragonite studies (n = 19)	4.9665 ± 0.008	7.9677 ± 0.013	5.7496 ± 0.0042	227.52 ± 0.76
Ranges	4.948–4.9856	7.9427–8.0103	5.7413–5.7626	225.75–229.48
All Biogenic aragonite studies (n = 23)	4.966 ± 0.0073	7.9681 ± 0.0119	5.749 ± 0.0042	227.48 ± 0.71
Ranges	4.948–4.9856	7.9427–8.0103	5.7413–5.7626	225.75–229.48
Synthetic aragonites (n = 2)	4.9613 ± 0.0007	7.9698 ± 0.0002	5.7437 ± 0.0007	227.11 ± 0.07
Ranges	4.9596–4.967	7.961–7.9703	5.7379–5.7441	226.649–227.2308
Geological studies (n = 12)	4.9622 ± 0.0021	7.9673 ± 0.0027	5.742 ± 0.0017	227.02 ± 0.16
Ranges	4.9596–4.967	7.961–7.9703	5.7379–5.7441	226.649–227.231

All individual Rietveld refinements from this study are listed in Supplementary Table 1. See Supplementary Table 2 for a compilation of values and references for previous studies

Instrumentation and analysis

X-ray diffraction

Powder X-ray diffraction (XRD) was conducted on a Rigaku D/MAX Rapid II micro X-ray diffractometer with a 2D imaging plate detector in the Hansel Lab, Woods Hole Oceanographic Institution using Mo Kα radiation (λ = 0.71069 Å). Samples were run for 10 min with omega fixed at 0° and phi rotating at 1°/s. Four sample replicates were run for each sample. XRD image files were background-corrected (manual setting = 5) and integrated into intensity versus 2θ patterns from 3.0 to 45.0 2θ degrees and 81.6337–430.00 β using 2DP software.

For the experimental setup, all samples were gently reground in an agate mortar and pestle to keep methods consistent between coral and non-coral samples. Powders were mounted in the lollipop method on Kapton tips by MiTeGen by using a very thin layer of mineral oil on the tips. For more details on the X-ray diffraction methods, see the Supplementary Materials, Extended Materials and Methods.

Rietveld refinement analysis

Rietveld refinement analysis determined unit-cell parameters by a least-squares fitting of the whole XRD pattern against a known model structure. Rietveld refinement analysis was performed using full-patterns from 8 to 44 2θ degrees (Mo radiation) using GSASII (Toby and Von Dreele 2013). We used a Chebyschev polynomial to model the background and previously reported aragonite (Antao

and Hassan 2009) and calcite (Markgaf and Reeder 1985) as model structures. Errors in Rietveld refinements were represented as estimated standard deviations (esd's) and exceeded standard deviations between sample replicates. It is important to note that esd's rely solely on counting statistics of the refinement and may underestimate the true error by up to an order of magnitude (Bish and Post 1989); however, such larger errors would still be smaller than the consistent crystallographic results we observed in this study. We measured four sample replicates to portray the range of Rietveld refinement results. For additional details on the Rietveld refinement analysis, see the Supplementary Materials, Extended Materials and Methods.

Raman spectroscopy

Powdered samples were measured for Raman spectroscopy at the Centre for Microscopy, Characterisation, and Analysis (CMCA) at the University of Western Australia with a WITec Alpha300 RA + confocal Raman microscope detailed in DeCarlo et al. (2017, 2018). The instrument uses an Andor iDUS 401 CCD detector maintained at − 60 °C, and measurements were made using a 785 nm laser, 20 × objective with numerical aperture of 0.5, and a 1200 mm^{-1} grating with a ∼ 1.2 cm^{-1} spectral resolution. FWHM measurements were corrected using repeated analyses of JCp-1 as a consistency standard (FWHM of 3.52 based on DeCarlo et al. 2018). Background fluorescence signals from organics in the aragonite samples were quantified at the base of the v_1 peak (see interpretation of Raman fluorescence in DeCarlo et al. 2018), which should be sufficient for observing relative differences in fluorescence between samples.

Inductively coupled plasma mass spectroscopy (ICP-MS)

Trace metal concentrations were measured using an iCAP ICP-MS at the Woods Hole Oceanographic Institution. Samples were digested with a solution of 5% trace metal grade nitric acid (J.T. Baker ULTREX® II Ultrapure Reagent) with Milli-Q water and a 2 ppb In spike in trace metal-cleaned 15 mL Falcon centrifuge tubes. The JCp-1 *Porites* sp. reference coral (Okai et al. 2002) was measured alongside the other samples in this study, as a standard for trace element to Ca ratios and to account for matrix effects, over the course of the ICP-MS run (Hathorne et al. 2013). Each measurement was taken as an average of ten analytical replicates. Due to limited sample quantities, only one sample replicate was run for each sample.

Statistics

Student *t*-tests (equal variance) and Welch's *t*-tests (unequal variance) were run on XLSTATS to determine whether groups of aragonites could be considered significantly similar ($p > 0.05$) or distinct ($p < 0.05$) based on crystallography and chemistry (all tests listed in the Supplementary Materials). We used Levene's tests for determining homogeneity of variances and Kolmogorov–Smirnov tests to confirm normality of residuals. Only the Raman background fluorescence values for the "all corals" group did not follow a normal distribution. Linear regressions and Pearson correlations were also run on XLSTATS and values for p, r (Pearson correlation coefficients), and r^2 (coefficients of determination) for all samples and variables are presented in the Supplementary Materials.

Results

Coral aragonite crystal structures and comparisons to other aragonites

Crystallographic measurements taken by micro-powder X-ray diffraction (XRD) confirm that all of the samples measured are predominantly aragonite (Fig. 1). Some coral samples exhibit small calcite (104) XRD peaks (Fig. 1, red arrows), indicating up to an ∼ 8% calcite phase contribution, as determined by dual-phase Rietveld refinements (Supplementary Table 1).

Despite the visual similarity of the XRD fingerprints, whole-pattern Rietveld refinement analyses allow us to determine the dimensions of the smallest possible building block for the mineral aragonite: the unit cell. These Rietveld refinement results show how the length of each axis (*a*, *b*, and *c*) in the aragonite unit cell contributes to the overall unit-cell volume in a way that unveils that there are marked differences in crystal structure between different forms of aragonite (corals, synthetic, geologically formed) (Table 1; Fig. 2a; Supplementary Table 1). The *c*-axis is defined as the axis perpendicular to the trigonal planar carbonate groups in the aragonite unit cell and is usually the fastest-growing axis (Fig. 2a). Overall, we observe that the average values for unit-cell parameters in this study fall within the range of refinement values obtained in previous studies, which were determined by various methods (Table 1, Supplementary Table 2). Across all samples, the *c*-axis length of the orthorhombic aragonite structure has the most overall impact on aragonite unit-cell volume
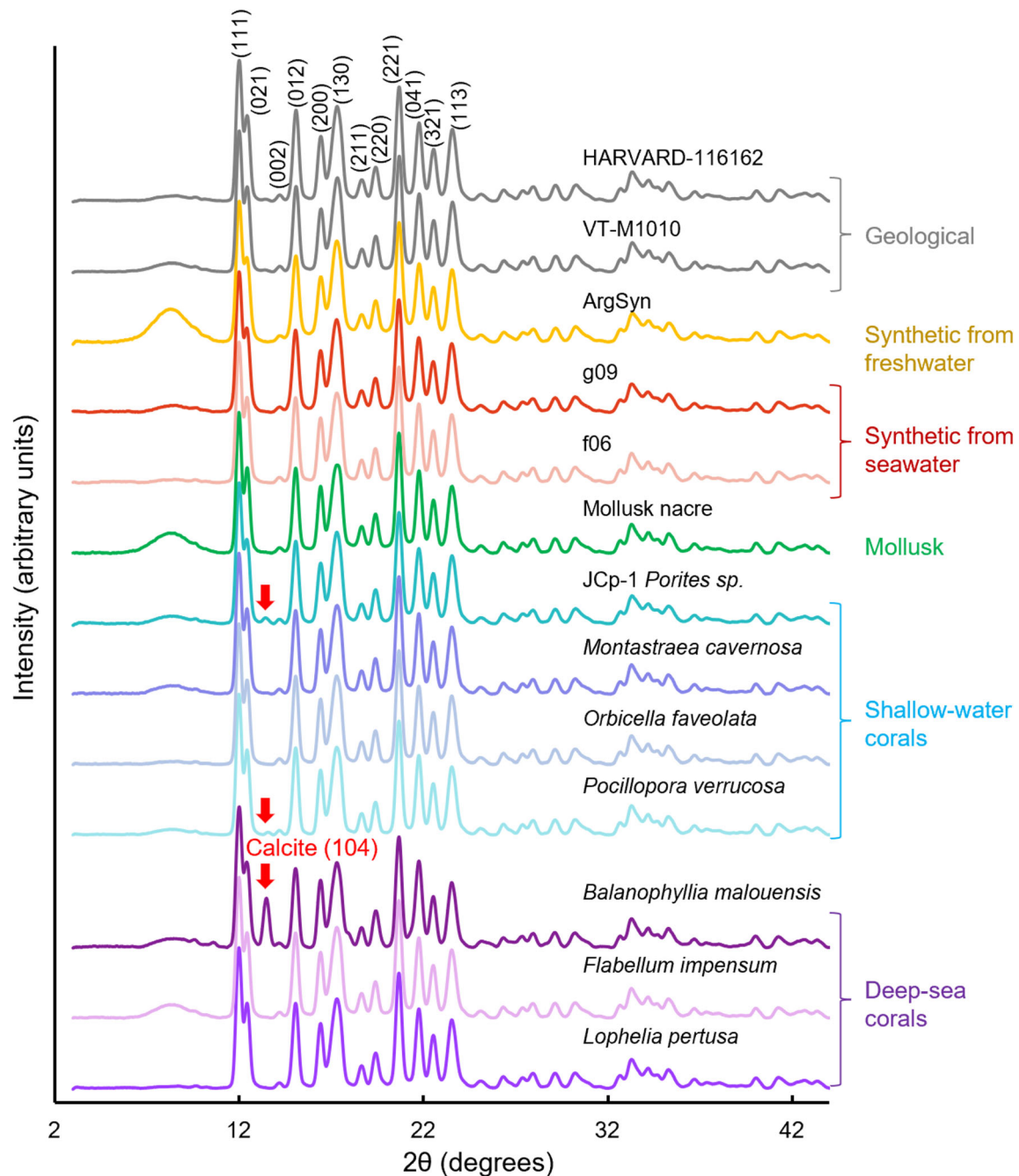
Fig. 1 Representative XRD patterns of aragonite formed by deep-sea corals (violet), shallow-water corals (blue), mollusk nacre (green), synthetic aragonites precipitated from seawater (red) and freshwater (yellow), and geological processes (grays) using Mo Kα radiation (λ = 0.71069 Å). Miller indices are labeled on the HARVARD-116162 XRD pattern, and all patterns are normalized to the (111) peak heights. Calcite (104) peaks are highlighted with red arrows on samples with visible calcite contents

(Fig. 2b r^2 = 0.88). Relationships of unit-cell volumes with the a- and b-axis lengths are slightly less robust (Fig. 2b r^2 = 0.77 and r^2 = 0.56, respectively).

Figure 3 illustrates how unit-cell parameters of different aragonites compare to one another side-by-side. (Relative shifts are illustrated in Supplementary Fig. 1.) Within the subset of coral samples (Fig. 3, range highlighted in gray), we observe that coral samples are crystallographically

similar to one another. Student t tests show that unit-cell volumes, and c-axis lengths do not vary significantly between DSACs (violet circles) and STZCs (blue squares; Fig. 3, Table 1, see Supplementary Table 3 for all statistical tests). STZCs do, however, have significantly longer b-axis lengths than DSACs (p = 0.0009), which can be weakly related to carbonate bonding environments (Supplementary Fig. 2, see Supplementary Table 3 for t-tests
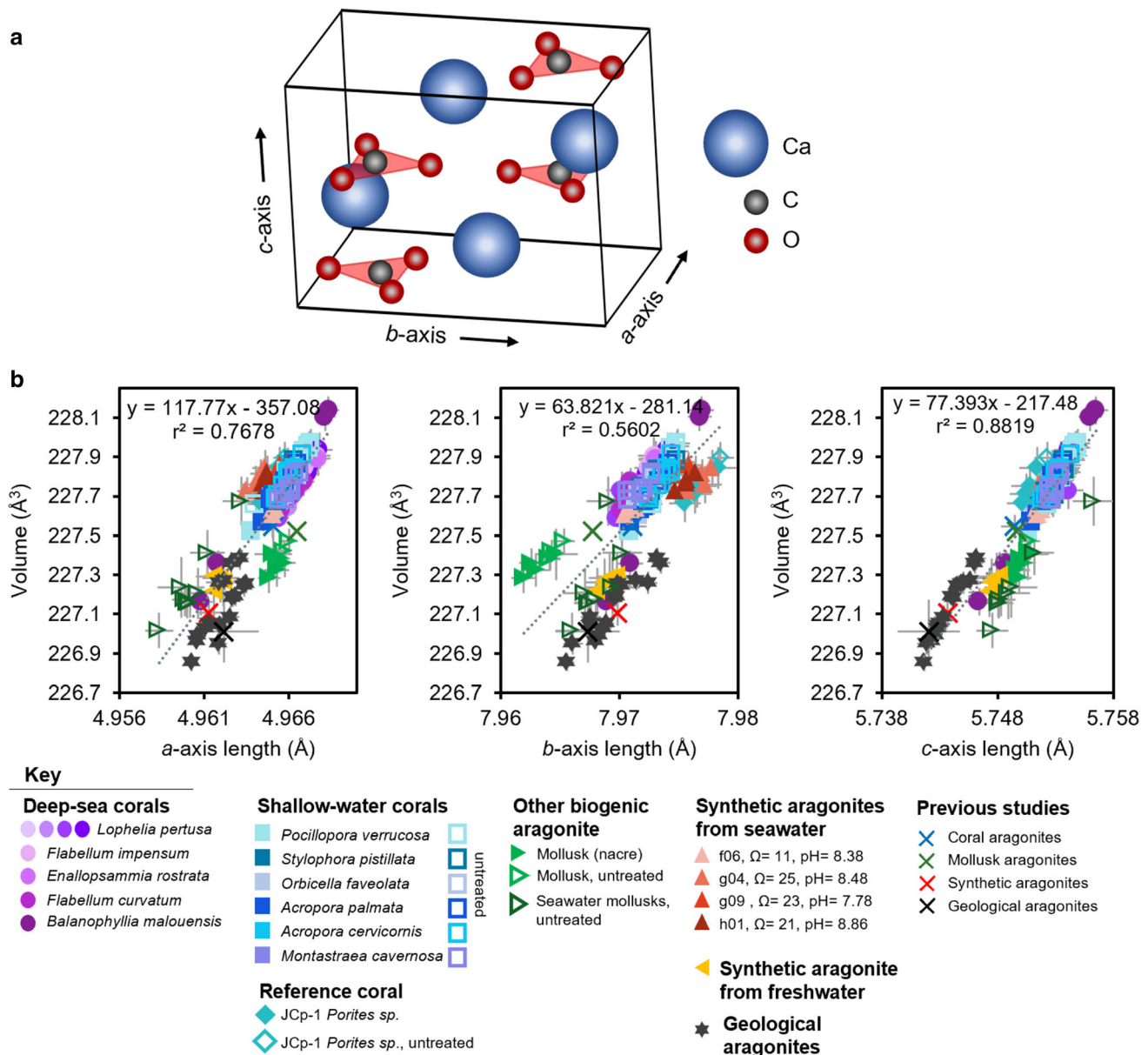
Fig. 2 a Illustration of the aragonite (CaCO$_3$) unit cell with labeled axes, modified from Farfan et al. (2018). The illustration is not to scale. **b** Shifts in overall aragonite unit-cell volume driven by anisotropic elongations of *a*-, *b*-, and *c*-axes for all samples measured in this study and for mean values compiled from previous studies. Trend lines for simple regressions are plotted in gray dotted lines. Error bars represent estimated standard deviations calculated by Rietveld refinements

and 4 for linear regressions and Pearson correlations). Compared to a previous coral aragonite study (Fig. 3, blue "*x*"; Stolarski et al. 2007), our observed coral aragonite unit-cell parameters are similar, with the exception of relatively longer coral *c*-axis lengths.

Mollusk aragonites from marine localities and from an unknown locality (Fig. 3, green, right-facing triangles) have slightly smaller ($p < 0.0001$) unit-cell volumes compared to the coral aragonites. This difference is also reflected across all three unit-cell axes.

Crystallographic similarities exist between coral aragonites and synthetic aragonites precipitated from aragonite-supersaturated filtered natural seawater (Fig. 3, red triangles, sample precipitation methods described in DeCarlo et al. 2015 and Holcomb et al. 2016). Student *t*-tests confirm that coral aragonite and seawater synthetic aragonite unit-cell parameter groups are statistically similar in unit-cell volume and *c*-axis length. Yet, unit-cell parameters are similar along all three axis lengths only for a seawater synthetic aragonite (sample f06, represented as peach triangles in figures) that was precipitated at an aragonite
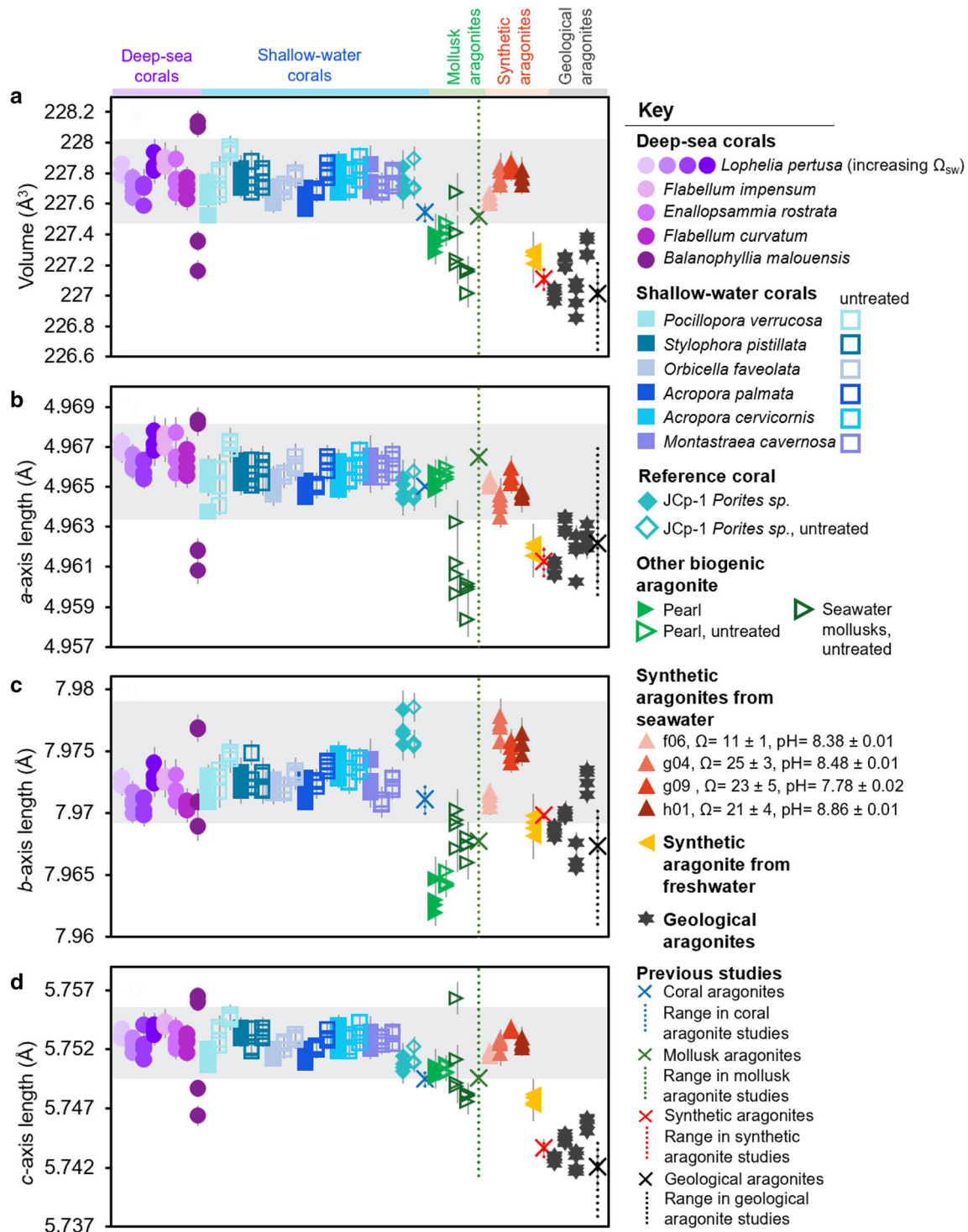
Fig. 3 Unit-cell parameters for all aragonites calculated in this study by whole-pattern Rietveld refinements are plotted to highlight the similarities and differences between aragonites formed by different methods (corals, synthetics, etc.). Unit-cell parameters are expressed as **a** unit-cell volumes, **b** *a*-axis lengths, **c** *b*-axis lengths, and **d** *c*-axis lengths. Light gray boxes highlight the range of values for the coral species measured in this study, excluding outlier *Balanophilia*

malouensis. Error bars represent estimated standard deviations calculated by Rietveld refinements. "*X*" markings with dashed lines represent the averages and ranges, respectively, of unit-cell parameters reported in previous studies. Values are all listed in Supplementary Table 1, and all values are plotted as ΔParameter$_{(Sample - GeologicalAragonite)}$/Parameter$_{GeologicalAragonite}$ in Supplementary Fig. 1

saturation state similar to that of coral calcifying fluid ($\Omega_{Arg} = 11 \pm 1$). In contrast, significant differences in a- and b-axis lengths are observed between coral aragonite and the other seawater synthetic aragonites precipitated at higher saturation states.

Coral aragonites are most crystallographically different from geologically formed aragonites in this study (Fig. 3, black stars) with significantly larger unit-cell volumes and longer a-, b-, and c-axes. Coral aragonites are also crystallographically distinct from a synthetic aragonite precipitated from a freshwater solution (Fig. 3, yellow triangles). Instead, the unit-cell values of this freshwater synthetic aragonite align closely with the geological aragonites measured in this study.

Raman-based carbonate bonding environments and background fluorescence

Raman spectroscopy similarly reveals additional information about the aragonite crystal structures by probing the bonding environments of the trigonal planar carbonate groups within the aragonite unit cell. Here, we focus on the position and the full-width at half-maximum (FWHM) of the dominant ν_1 symmetrical stretching vibrational mode peak (Supplementary Table 5). Any shifts in the frequency of bond vibrations (peak positions) or tilting of the trigonal planar carbonate group (peak widths) are an indication of structural disorder and complement our XRD-based unit-cell measurements. The FWHM of the ν_1 peak is also used to empirically derive Raman-based aragonite saturation states of formation Ω_{Arg} (or Ω_{cf} for coral calcifying fluid, DeCarlo et al. 2017). This relationship is most likely driven by more perfect crystals nucleating and growing more slowly from less-saturated solutions and exhibiting thinner ν_1 FWHMs, versus more disordered crystals forming more quickly from higher-saturated solutions and yielding wider ν_1 FWHMs (Farfan et al. 2018).

We observe that our array of samples mostly cluster based on formation source, with increasing unit-cell volumes trending weakly with increasing ν_1 FWHM ($r^2 = 0.27$; Fig. 4a) and Raman-derived Ω_{Arg} ($r^2 = 0.15$; Fig. 4b). Based on the ν_1 FWHM measurements, geological aragonites are estimated to have formed at the lowest Ω_{Arg}, followed by corals, the mollusk sample, the freshwater synthetic sample, and finally the set of seawater synthetic aragonites that were precipitated at higher Ω_{Arg} (Fig. 4a, b). Unlike the close similarities in unit-cell structure between coral aragonites and seawater synthetic aragonites, carbonate bonding environments separate the seawater aragonites precipitated at higher Ω_{Arg} from the cluster of coral samples (red triangles, Fig. 4a, b). However, we do observe that sample f06 precipitated at lower Ω_{Arg} clusters within the coral aragonite samples in plots of

unit-cell volume versus ν_1 FWHMs and Raman-derived Ω_{Arg} (peach triangles, Fig. 4a, b).

In addition to carbonate bonding environments, we also measured the relative background luminescence of our Raman spectra (herein referred to as fluorescence, per the nomenclature used in previous studies) as a proxy for organic content in our samples (Von Euw et al. 2017; DeCarlo et al. 2018). This proxy assumes that fluorescence is primarily attributed to organics and not to other major fluorescent impurities, and that all biomolecular compounds luminesce compared to non-fluorescent, pure aragonite. We observe significantly higher background fluorescence Raman signals in mollusk aragonite for both untreated and bleach-treated samples (Fig. 4c, green right-facing triangles) compared to corals and all other forms of aragonite.

Trace element incorporations

Across all of the samples, B/Ca ($r^2 = 0.47$) and Sr/Ca ($r^2 = 0.65$) ratios positively relate to increasing unit-cell volumes (Fig. 5a, c). In contrast, Mg/Ca ratios ($r^2 = 0.13$) and Ba/Ca ratios ($r^2 = 0.31$) are weakly negatively related to unit-cell volume and are mostly driven by exceptionally high values measured in the freshwater synthetic aragonite and some geological aragonites in our plots (Fig. 5b, d).

Within the subset of coral samples, crystal structure and carbonate bonding environment signatures are separated by STZC and DSAC groups and are strongly linearly related to metal/Ca ratios calculated from trace element concentrations measurements via inductively coupled plasma mass spectrometry (ICP-MS) analyses (Fig. 6, Supplementary Fig. 3; Supplementary Table 6). We observe strong relationships between wider ν_1 FWHM and increasing Mg/Ca ($r^2 = 0.47$), and an opposite trend with B/Ca and Sr/Ca ratios (Fig. 6a–c). Not only are ν_1 FWHMs widened by Mg incorporations, likely induced by more disorder in the crystal structure, but we also see that the frequency of symmetric stretching vibrations in the carbonate group increases, as is represented by increasing peak positions for the ν_1 mode as a function of increasing Mg/Ca ratios (Fig. 6f). Again, B/Ca and Sr/Ca ratios show the opposite relationship as a function of ν_1 peak positions (Fig. 6d, e). While the spectral resolution of the Raman measurements limits the precision of the ν_1 peak position values, the relative shifts in peak positions trend particularly well with element/Ca ratios in this study ($r^2 = 0.4578–0.6992$).
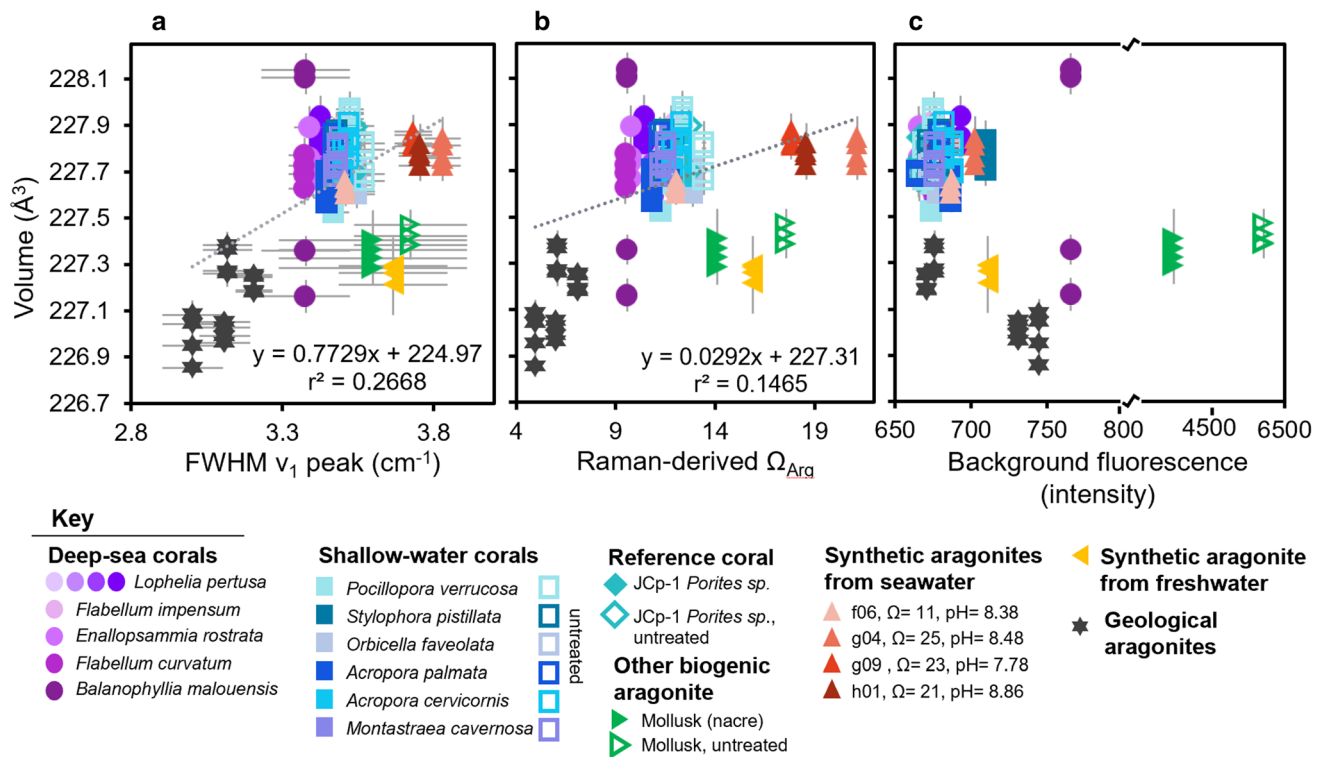
Fig. 4 Unit-cell volume of all aragonite samples as a function of **a** FWHM v_1 peak, **b** Raman-derived Ω_{Arg}, and **c** Raman background fluorescence intensity. Error bars represent estimated standard deviations calculated by Rietveld refinements for unit-cell volume and standard errors for the FWHM of the v_1 peak

Discussion

Crystallographic signatures are remarkably similar between scleractinian corals from different ocean environments

This study is the first to perform Rietveld refinements for a wide array of coral species and to systematically compare these coral crystallographic signatures to a range of aragonites formed by other means. In doing so, we find significant and reproducible similarities and differences among aragonites (see Methods under *X-ray diffraction* and *Rietveld Analysis* for justification of refinement confidence).

One of the most notable results is that despite the wide span of coral species and ocean environments represented (temperatures ranging from − 2 to 35 °C, ocean depths of ∼ 0 to 5000 m, and seawater aragonite saturation states (Ω_{sw}) of < 1 to − 4, McCulloch et al. 2012b), corals make aragonite with remarkably consistent crystal structure parameters and chemistries, especially relative to aragonites formed by other means (Supplementary Table 1). This observation supports previous research findings that scleractinian corals control their calcifying space carbonate chemistry, specifically by raising their internal Ω_{cf} up to ∼ 8 to 25, despite living in surrounding seawater with

much lower Ω_{Arg} (Cohen et al. 2009; McCulloch et al. 2012a, b; Sevilgen et al. 2019).

While small differences in volume and unit-cell axis lengths may have strong effects on the material properties of aragonite, such as solubility, toughness, and other material properties that could directly impact coral skeletal health (e.g., Bischoff et al. 1983; Gutjahr et al. 1996), the lack of change in unit-cell volume and *c*-axis lengths between DSACs and STZCs suggests that the material properties of coral aragonites are consistent between these vastly different environments. Smaller but noticeable trends in the *b*- and *a*-axes may still offer physicochemical signals in coral aragonites that could be useful in delineating differences in the surrounding chemical environment and/or pointing out perhaps subtle nuances in the controls on aragonite formation by these different coral groups (e.g., rates, trace element substitution, types of organic templates).

We assume that crystallographic outliers, *B. malouensis* and reference JCp-1, are different from the other corals due to the abnormally high calcite content in *B. malouensis* (may indicate diagenesis) and potentially by the processing methods used on JCp-1 (extensive grinding for four days by ball mill may have introduced enough heat to lead to annealing, Okai et al. 2002; DeCarlo et al. 2018). We do not observe any significant differences in crystallography
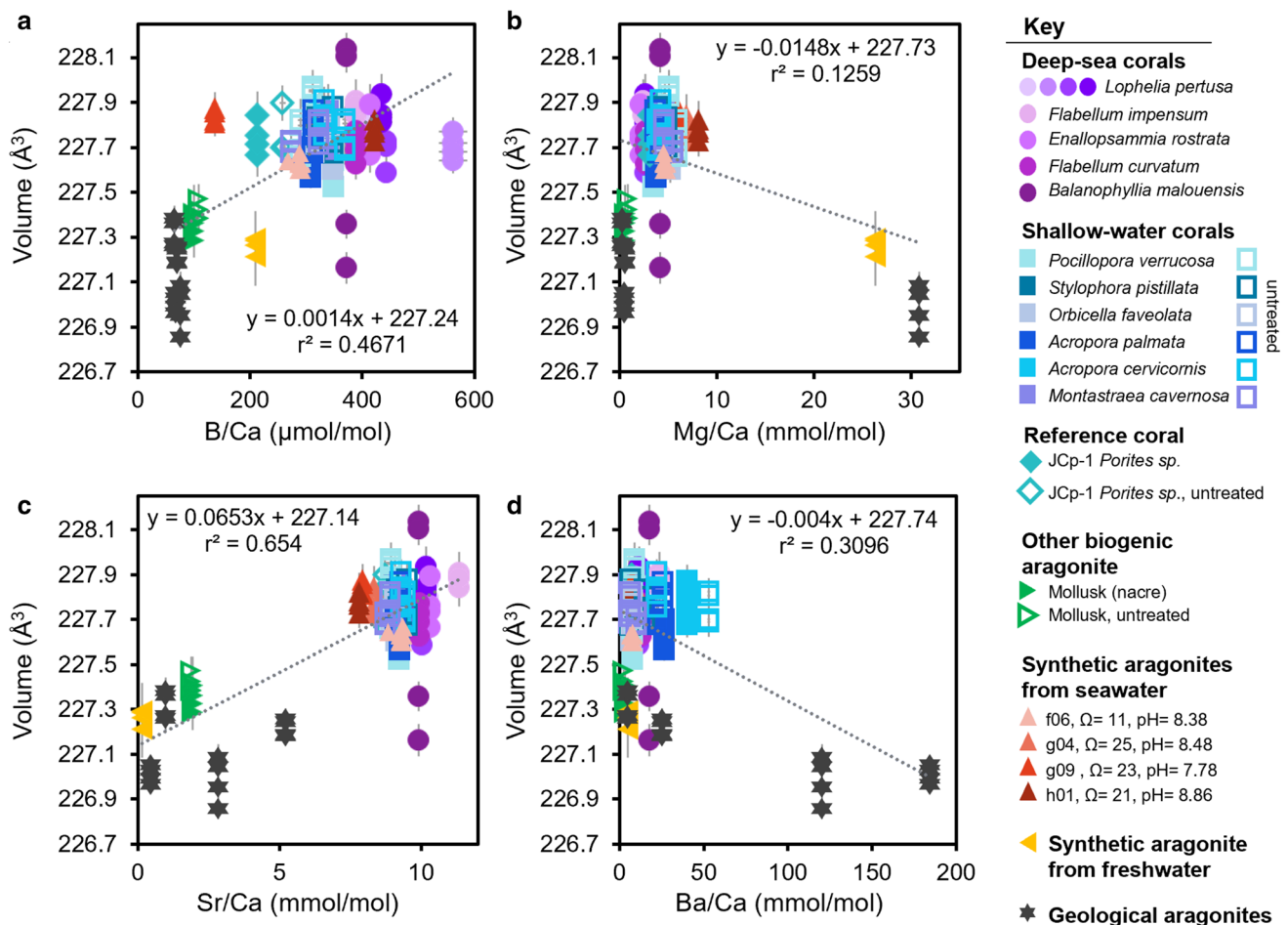
Fig. 5 Shifts in unit-cell volume in all samples as a function of **a** B calculated from [11]B, **b** Mg calculated from [24]Mg, **c** Sr calculated from [88]Sr, and **d** Ba calculated from [138]Ba. Ratios are calculated based on metal/Ca ratios in the JCp-1 reference coral (Hathorne et al. 2013). Linear regression p values and coefficients of determination are in Supplementary Table 4. Error bars represent estimated standard deviations

between untreated and bleach-treated coral aragonite samples, with the possible exception of slightly different *c*-axis lengths (Supplementary Table 3).

Coral aragonites are not crystallographically equivalent to mollusk aragonites

Despite coral skeletons and many mollusk shells being composed of predominantly aragonite, our crystallographic observations suggest that not all biological aragonites should be treated as having equivalent crystal structures. Previous studies using mollusk aragonite as a model system (Pokroy et al. 2004, 2007; Antao 2012; Rao et al. 2016; Roger et al. 2017) to represent biogenic aragonite have observed systematic crystallographic differences between geological and biogenic aragonites and assumed that these observations extend to coral aragonites. However, mollusk aragonites in previous studies displayed shorter *b*-axes lengths and elongated *a*- and *c*-axes compared to

geological aragonites, whereas in this study, the *b*-axis lengths are more variable (Fig. 3). Still, we see significant differences along all three axis lengths between mollusk and coral aragonites in this study (Fig. 3, $p < 0.001$).

These crystallographic differences between coral and mollusk aragonite echo other key differences between coral and mollusk aragonite. First, previous studies estimate that mollusk aragonite has a 0.1–5 wt% organic content which is $5 \times$ higher than estimates for coral aragonite (Gilbert et al. 2005). Our study confirms this observation by our background fluorescence observations as a proxy for organic contents (Fig. 4c). Since coral aragonites have consistently larger unit-cell volumes compared to mollusk aragonites, but smaller organic contents, it is unlikely that organics are responsible for crystal structure distortions in coral aragonite, as has been suggested for mollusks (Pokroy et al. 2004, 2007; Gilbert et al. 2005). Second, while changes in crystal morphology reflect growth environment and do not necessarily indicate differences in atomic
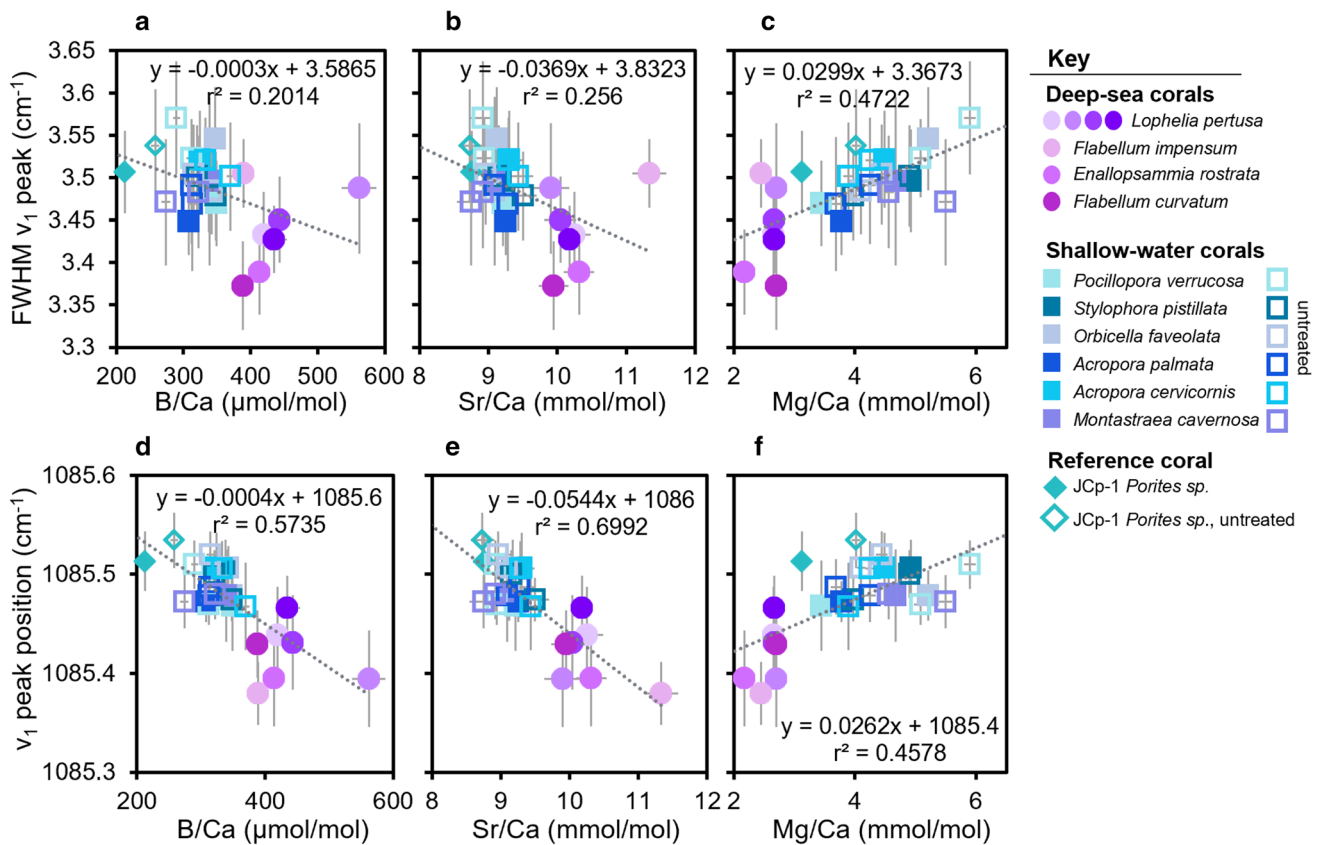
Fig. 6 Coral aragonite **a–c** v_1 Raman peak FWHMs, and **d–f** v_1 Raman peak positions as functions of B/Ca, Sr/Ca, and Mg/Ca ratios, respectively. Error bars represent standard errors for the Raman data and estimated standard deviations for the trace element data

structure, in this case, the observed structural differences between mollusk and coral aragonite are reflected in their different crystal habits. Specifically, coral aragonites grow into acicular needle-like crystals which extend along the *c*-axis (Holcomb et al. 2009), whereas mollusk nacre is composed of stacked, flat aragonite platelets that are stunted along the *c*-axis (Gilbert et al. 2005).

Seawater synthetic aragonites may serve as scleractinian coral aragonite crystallographic analogs

While crystal structure does not necessarily reflect crystal morphology, in this case, these crystallographic similarities complement previous studies that have documented the morphological and chemical similarities between coral and seawater-precipitated synthetic aragonites, both of which form acicular needle-like crystals (Constantz 1986; Gaetani and Cohen 2006; Holcomb et al. 2009; DeCarlo et al. 2017, 2018). These similarities likely indicate that physicochemical processes are guiding controls in the formation of scleractinian coral aragonite. While corals exert control on the saturation state conditions and likely biomolecule mediated nucleation process, subsequent

controls on the crystal growth and aggregation appear to operate under fundamental abiotic precipitation principles. As the seawater synthetic aragonites were precipitated in filtered natural seawater, the only organic carbon present was dissolved organic carbon (DOC) that could be incorporated within the structure, but likely not as a templating polymer. Further, these synthetic aragonites were not precipitated in the presence of any coral proteins that could mediate the nucleation process.

The main caveat to using seawater synthetic aragonites as analogs to scleractinian coral aragonite is that these synthetics must be precipitated in environments similar to coral calcifying fluids. Of our seawater synthetic aragonites, only sample f06 ($\Omega_{\text{Arg}} = 11 \pm 1$) represents a scenario mimicking previous δ^{11}B-based and Raman-based estimates for DSAC $\Omega_{\text{cf}} = 8.5$–13 and STZC $\Omega_{\text{cf-}} = 10.8$–25 (McCulloch et al. 2012a, b; DeCarlo et al. 2017). We find that both the crystal structures and bonding environments of coral aragonites are remarkably similar to this sample f06 analog ($p > 0.06$ for all XRD and Raman measurements). Nevertheless, a greater number of synthetic aragonites precipitated at a range of coral-relevant Ω_{Arg} should be investigated in the future to confirm that this observation extends beyond this one sample.

While previous crystallographic studies comparing coral aragonites to synthetic aragonites utilized freshwater solutions (Stolarski et al. 2007; Sun et al. 2017), these synthetics are more crystallographically similar to geologically formed aragonites, making them less suitable analogs for studies looking to compare biological versus abiological influences on coral aragonite. Instead, we propose that seawater-precipitated synthetic aragonites may provide a useful means to study coral aragonite crystal structures and material properties under varying environmental stress conditions due to the greater ease in laboratory preparation. Beyond this study, these crystallographic and chemical signatures may become a useful resource in resolving other geochemical problems, such as pinpointing the genesis of aragonite samples from unknown origins.

Physicochemical variables and ionic strength drive crystallographic distortions

Major crystallographic differences between aragonites are most likely tied to ionic strength and other physicochemical variables which influence trace element incorporation into aragonite. Across Fig. 3, we observe that the aragonites with the largest unit cells, particularly coral aragonites and seawater aragonites, were precipitated from coral calcifying fluids and seawater solutions that have particularly high ionic strengths. Considering how recent experiments observed that Na from saltwater can be trapped in aragonite spherulites (Boon et al. 2020), future studies could explore the role of Na and salinity on aragonite unit-cell parameters.

Of the elements we measured, higher Sr/Ca and B/Ca ratios appear to drive the larger unit-cell volumes across all aragonites (Fig. 5a, c), yet have narrower FWHM ν_1, indicating less disorder on the carbonate bonding environments (Fig. 6a–e). This may indicate that the position of Sr and B incorporations in the aragonite structure is along the c-axis direction such that these incorporations cause distortions perpendicular to the trigonal planar carbonate group and do not cause net disruptions along the a- and b-axes. In contrast, Mg incorporations are known to lead to shorter unit-cell a- and c-axis lengths in synthetic aragonites (also weakly seen in our study, Supplementary Fig. 3c; Boon et al. 2020). Similarly, we only observe weak crystal structure shifts along the a- and b-axes of the unit cell as a function of trace element incorporations in the coral-only subgroup (Supplementary Fig. 3). The difference in behavior between Mg and Sr incorporations in aragonite can also be explained by extended X-ray absorption fine structure spectroscopy (EXAFS) measurements which show that metal–oxygen distances are slightly longer for Sr and much shorter for Mg, compared to Ca-oxygen distances (Finch and Allison 2007).

Similarities in unit cell volume and broad trace element concentrations between coral aragonite and seawater synthetic aragonite (Fig. 5) support previous studies that suggest scleractinian coral skeleton trace element chemistry reflects seawater chemistry, which has been adjusted by the coral to favor precipitation and continued growth in the calcifying fluid space (Holcomb et al. 2009; Gagnon et al. 2012). This strong geochemical influence is also observed in experiments on juvenile scleractinian corals, which when grown in Cretaceous-like "calcite sea" seawater with lower Mg/Ca ratios subsequently precipitated calcite over aragonite in the new skeletal growth (Higuchi et al. 2014).

Crystallographic nuances in coral aragonites can be traced with trace elements

Within the coral-subgroup, strong relationships between carbonate bonding environments in coral aragonites as a function of trace element concentration suggest clear links between trace element incorporations in the aragonite crystal structures and the physicochemical conditions in which the different corals grew (e.g., mineral saturation state, temperature, crystal grow rate, crystal structure disorder; Fig. 6, Supplementary Fig. 3; Supplementary Table 6). Our trace element incorporation results corroborate previous studies using bulk trace element analyses and isotopic (and other) proxies that reported DSACs growing in cold, low Ω_{Arg} seawaters, form skeletons at lower Ω_{cf} (McCulloch et al. 2012a, b) and contain higher B/Ca and Sr/Ca ratios, but lower Mg/Ca ratios, than STZC aragonite (reviewed in Cohen and Gaetani 2010). B/Ca and Sr/Ca ratios are also known to co-vary within coral skeletons (Hart and Cohen 1996). Considering that these are environmental samples subjected to many variables, we find that the trends between carbonate bonding environments and trace element incorporations are particularly strong and have the potential to be used as independent Raman-based (and possibly X-ray diffraction-based, Farfan et al. 2018) mineral proxies for helping to estimate trace elements, Ω_{cf} (DeCarlo et al. 2017), and other environmental signals. Future studies should consider calibrating Raman and X-ray diffraction-based measurements to controlled aragonite precipitation experiments doped with different trace elements.

Combining our results with previous environmental trace element and experimental carbonate studies, we offer the following potential causes for variable metal/Ca ratios in these different corals. While B incorporation in aragonite is known to be influenced by pH, temperature, and crystal growth rate, our observed higher B/Ca ratios in DSACs (Fig. 6a, d) mirror the temperature dependence of the B partition coefficients (K_D) in coral aragonites from previous studies. DSACs growing in low pH and cold

waters (< 12 °C) typically have a much higher estimated boron K_D values ($K_D \times 1000 = \sim 30$) than STZCs growing at higher pH and sea-surface temperatures (SST) of > 20 °C ($K_D \times 1000 = \sim 5 - 15$, Douville et al. 2010; Mavromatis et al. 2015). Sr/Ca ratios are proportional to the concentration of dissolved Sr in seawater (Ferrier-Pagès et al. 2002) and commonly used as a temperature proxy, with higher ratios indicating colder deep-sea water conditions reflected in DSAC aragonites (Kinsman and Holland 1969; Gaetani and Cohen 2006). In contrast, the lower Mg/Ca ratios in DSACs are likely a consequence of the incompatibility of the smaller ionic radius of Mg^{2+} in the aragonite structure (Boon et al. 2020). DSAC skeletons grow at substantially slower rates than STZC skeletons (~ 0.07–5 mm/y versus ~ 10–20 mm/y, Adkins et al. 2004; McCulloch et al. 2012a), presumably due to low surrounding seawater Ω_{Arg} and lower temperatures (Farfan et al. 2018). If we assume that slower skeletal growth rates reflect slower rates of aragonite crystallization, this would result in lower crystalline disorder, fewer structural imperfections, and fewer incompatible substitutions of Mg^{2+} for Ca^{2+} in DSAC aragonites (Gabitov et al. 2008; DeCarlo et al. 2015; Fig. 6c, f). Because Sr^{2+} has a more similar-sized radius to Ca^{2+}, it is a more compatible substitute and observed in higher concentrations in DSACs (Fig. 6b, e). Overall, we suggest that growth rate plays a secondary role to local environmental conditions because we observe distinctions between DSAC and SZTC aragonites that span coral species with very different morphologies in each category (Figs. 5, 6). However, we expect that if we were to repeat this crystallographic exercise across different microstructures of a single coral skeleton (such as rapid accretion deposits versus thickening deposits, or centers of calcification versus fibers), we may observe shifts in crystallographic parameters and bonding environments that mirror the known changes in trace element chemistry across these features (ex: Meibom et al. 2008; Allison et al. 2010; DeCarlo et al. 2018).

By linking crystal structure and carbonate bonding environments with trace element incorporations, we propose that these crystallographic signatures have the potential to be used as mineral-based environmental proxies to track environmental shifts recorded in coral aragonite. Still, overall similarities between DSAC and STZC aragonites suggest that scleractinian corals hold immense control over their skeletal aragonite formation.

Declarations

References

Adkins JF, Henderson GM, Wang SL, O'Shea S, Mokadem F (2004) Growth rates of the deep-sea scleractinia *Desmophyllum cristagalli* and *Enallopsammia rostrata*. Earth Planet Sc Lett 227:481–490

Allison N, Finch AA, EIMF, (2010) δ11B, Sr, Mg and B in a modern Porites coral: the relationship between calcification site pH and skeletal chemistry. Geochim Cosmochim Acta 74:1790–1800

Antao SM (2012) The crystal structure of a biogenic aragonite from the nacre of an ammonite shell. RSC Adv 2:526–530

Antao SM, Hassan I (2009) The orthorhombic structure of CaCO₃, SrCO₃, PbCO₃ and BaCO₃: Linear structural trends. Can Mineral 47:1245–1255

Benzerara K, Menguy N, Obst M, Stolarski J, Mazur M, Tylisczak T, Brown GE Jr, Meibom A (2011) Study of the crystallographic architecture of corals at the nanoscale by scanning transmission X-ray microscopy and transmission electron microscopy. Ultramicroscopy 111:1268–1275

Bischoff WD, Bishop FC, Mackenzie FT (1983) Biogenically produced magnesian calcite; inhomogeneities in chemical and physical properties; comparison with synthetic phases. Am Mineral 68:1183–1188

Bischoff WD, Sharma SK, MacKenzie FT (1985) Carbonate ion disorder in synthetic and biogenic magnesian calcites: a Raman spectral study. Am Mineral 70:581–589

Bish DL, Post JE (1989) Rietveld refinement of crystal structures using powder X-ray diffraction data. In: Bish DL, Post JE (eds) Modern powder diffraction, Rev Mineral Geochem 20:227–305

Blue CR, Giuffre A, Mergelsberg S, Han N, De Yoreo JJ, Dove PM (2017) Chemical and physical controls on the transformation of amorphous calcium carbonate into crystalline $CaCO_3$ polymorphs. Geochim Cosmochim Acta 196:179–196

Boon M, Rickard WD, Rohl AL, Jones F (2020) Stabilization of Aragonite: Role of Mg^{2+} and Other Impurity Ions. Cryst Growth Des 20:5006–5017

Cai WJ, Ma Y, Hopkinson BM, Grottoli AG, Warner ME, Ding Q, Hu X, Yuan X, Schoepf V, Xu H, Han C (2016) Microelectrode characterization of coral daytime interior pH and carbonate chemistry. Nat Commun 7:11144

Carpenter KE, Abrar M, Aeby G, Aronson RB, Banks S, Bruckner A, Chiriboga A, Cortés J, Delbeek JC, DeVantier L, Edgar GJ (2008) One-third of reef-building corals face elevated extinction risk from climate change and local impacts. Science 321:560–563

Caspi EN, Pokroy B, Lee PL, Quintana JP, Zolotoyabko E (2005) On the structure of aragonite. Acta Cryst B 61:129–132

Cohen AL, Gaetani GA (2010) Ion partitioning and the geochemistry of coral skeletons: solving the mystery of the vital effect. EMU Notes Mineral 11:377–397

Cohen AL, McCorkle DC, de Putron S, Gaetani GA, Rose KA (2009) Morphological and compositional changes in the skeletons of new coral recruits reared in acidified seawater: Insights into the biomineralization response to ocean acidification. Geochem Geophys Geosyst 10:1–12

Cohen AL, McConnaughey T (2003) Geochemical perspectives on coral mineralization. In: Dove P, Weiner S, De Yoreo J (eds). Biomineralization. Rev Mineral Geochem 54:151–187

Constantz BR (1986) Coral skeleton construction: a physiochemically dominated process. Palaios 152–157

Coronado I, Fine M, Bosellini FR, Stolarski J (2019) Impact of ocean acidification on crystallographic vital effect of the coral skeleton. Nat Commun 10:2896

Cuif JP, Dauphin Y (2005) The Environment Recording Unit in coral skeletons–a synthesis of structural and chemical evidences for a biochemically driven, stepping-growth process in fibres. Biogeosciences 2:61–73

De Yoreo JJ, Gilbert PU, Sommerdijk NA, Penn RL, Whitelam S, Joester D, Zhang H, Rimer JD, Navrotsky A, Banfield JF, Wallace AF (2015) Crystallization by particle attachment in synthetic, biogenic, and geologic environments. Science 349:498

DeCarlo TM, Gaetani GA, Holcomb M, Cohen AL (2015) Experimental determination of factors controlling U/Ca of aragonite precipitated from seawater: Implications for interpreting coral skeleton. Geochim Cosmochim Acta 162:151–165

DeCarlo TM, D'Olivo JP, Foster T, Holcomb M, Becker T, McCulloch MT (2017) Coral calcifying fluid aragonite saturation states derived from Raman spectroscopy. Biogeosciences 14:5253

DeCarlo TM, Ren H, Farfan GA (2018) The origin and role of organic matrix in coral calcification: insights from comparing coral skeleton and abiogenic aragonite. Front Mar Sci 5:170

Dickens B, Bowen JS (1971) Refinement of the Crystal Structure of the Aragonite Phase of $CaCO_3$. J Res Natl Stand Sec A 75A:27–32

Douville É, Paterne M, Cabioch G, Louvat P, Gaillardet J, Juillet-Leclerc A, Ayliffe L (2010) Abrupt sea surface pH change at the end of the Younger Dryas in the central sub-equatorial Pacific inferred from boron isotope abundance in corals (Porites). Biogeosciences 7:2445–2459

Farfan GA, Cordes EE, Waller RG, DeCarlo TM, Hansel CM (2018) Mineralogy of deep-sea coral aragonites as a function of aragonite saturation state. Front Mar Sci 5:473

Ferrier-Pagès C, Boisson F, Allemand D, Tambutté E (2002) Kinetics of strontium uptake in the scleractinian coral Stylophora pistillata. Mar Ecol Prog Ser 245:93–100

Finch AA, Allison N (2007) Coordination of Sr and Mg in calcite and aragonite. Mineral Mag 71:539–552

Foster T, Falter JL, McCulloch MT, Clode PL (2016) Ocean acidification causes structural deformities in juvenile coral skeletons. Sci Adv 2:1–7

Gabitov RI, Gaetani GA, Watson EB, Cohen AL, Ehrlich HL (2008) Experimental determination of growth rate effect on U^{6+} and Mg^{2+} partitioning between aragonite and fluid at elevated U^{6+} concentration. Geochim Cosmochim Acta 72:4058–4068

Gaetani GA, Cohen AL (2006) Element partitioning during precipitation of aragonite from seawater: a framework for understanding paleoproxies. Geochim Cosmochim Acta 70:4617–4634

Gagnon AC, Adkins JF, Erez J (2012) Seawater transport during coral biomineralization. Earth Planet Sci Lett 329–330:150–161

Gilbert PUPA, Abrecht M, Frazer BH (2005) The organic-mineral interface in biominerals. Rev Mineral Geochem 59:157–185

Gutjahr A, Dabringhaus H, Lacmann R (1996) Studies of the growth and dissolution kinetics of the $CaCO_3$ polymorphs calcite and aragonite II. The influence of divalent cation additives on the growth and dissolution rates. J Cryst Growth 158:310–315

Hart SR, Cohen AL (1996) (1996) An ion probe study of annual cycles of Sr/Ca and other trace elements in corals. Geochim Cosmochim Acta 60:3075–3084

Hathorne EC, Gagnon A, Felis T, Adkins J, Asami R, Boer W, Caillon N, Case D, Cobb KM, Douville E, Demenocal P (2013) Interlaboratory study for coral Sr/Ca and other element/Ca ratio measurements. Geochem Geophys Geosyst 4:3730–3750

Hennige SJ, Wicks LC, Kamenos NA, Perna G, Findlay HS, Roberts JM (2015) Hidden impacts of ocean acidification to live and dead coral framework. Proc R Soc Lond [biol] 282:1–10

Higuchi T, Fujimura H, Yuyama I, Harii S, Agostini S, Oomori T (2014) Biotic Control of Skeletal Growth by Scleractinian Corals in Aragonite–Calcite Seas. PLoS One 9:e91021

Hoegh-Guldberg O, Poloczanska ES, Skirving W, Dove S (2017) Coral reef ecosystems under climate change and ocean acidification. Front Mar Sci 4:158

Holcomb M, Cohen AL, Gabitov RI, Hutter JL (2009) Compositional and morphological features of aragonite precipitated experimentally from seawater and biogenically by corals. Geochim Cosmochim Acta 73:4166–4179

Holcomb M, DeCarlo TM, Gaetani GA, McCulloch M (2016) Factors affecting B/Ca ratios in synthetic aragonite. Chem Geol 437:67–76

Kinsman DJ, Holland HD (1969) The co-precipitation of cations with $CaCO_3$—IV. The co-precipitation of Sr^{2+} with aragonite between 16° and 96° C. Geochim Cosmochim Acta 33:1–17

Levi Y, Albeck S, Brack A, Weiner S, Addadi L (1998) Control over aragonite crystal nucleation and growth: an in vitro study of biomineralization. Chem Eur 4:389–396

Markgaf SA, Reeder RJ (1985) High-temperature structure refinements of calcite and magnesite. Am Mineral 70:590–600

Mass T, Drake JL, Haramaty L, Kim JD, Zelzion E, Bhattacharya D, Falkowski PG (2013) Cloning and characterization of four novel coral acid-rich proteins that precipitate carbonates in vitro. Curr Biol 23:1126–1131

Mavromatis V, Montouillout V, Noireaux J, Gaillardet J, Schott J (2015) Characterization of boron incorporation and speciation in calcite and aragonite from co-precipitation experiments under controlled pH, temperature and precipitation rate. Geochim Cosmochim Acta 150:299–313

McCulloch M, Trotter J, Montagna P, Falter J, Dunbar R, Freiwald A, Försterra G, Correa ML, Maier C, Rüggeberg A, Taviani M (2012a) Resilience of cold-water scleractinian corals to ocean acidification: Boron isotopic systematics of pH and saturation state up-regulation. Geochim Cosmochim Acta 87:21–34

McCulloch M, Falter J, Trotter J, Montagna P (2012b) Coral resilience to ocean acidification and global warming through pH up-regulation. Nat Clim Change 2:623

Meibom A, Cuif JP, Houlbreque F, Mostefaoui S, Dauphin Y, Meibom KL, Dunbar R (2008) Compositional variations at ultra-structure length scales in coral skeleton. Geochim Cosmochim Acta 72:1555–1569

Okai T, Suzuki A, Kawahata H, Terashima S, Imai N (2002) Preparation of a new Geological Survey of Japan geochemical reference material: Coral JCp-1. Geostand Newsl 26:95–99

Pokroy B, Quintana JP, El'ad NC, Berner A, Zolotoyabko E (2004) Anisotropic lattice distortions in biogenic aragonite. Nat Mater 3:900

Pokroy B, Fieramosca JS, Von Dreele RB, Fitch AN, Caspi EN, Zolotoyabko E (2007) Atomic Structure of Biogenic Aragonite. Chem Mater 19:3244–3251

Rao DV, Gigante GE, Kumar YM, Cesareo R, Brunetti A, Schiavon N, Akatsuka T, Yuasa T, Takeda T (2016) Synchrotron-based crystal structure, associated morphology of snail and bivalve shells by X-ray diffraction. Radiat Phys Chem Oxf 167:155–164

Roger LM, George AD, Shaw J, Hart RD, Roberts M, Becker T, McDonald BJ, Evans NJ Roger LM, George AD, Shaw J, Hart RD, Roberts M, Becker T, McDonald BJ, Evans NJ (2017) Geochemical and microstructural characterisation of two species of cool-water bivalves (*Fulvia tenuicostata* and *Soletellina biradiata*) from Western Australia. Biogeosciences 14:1721–1737

Sevilgen DS, Venn AA, Hu MY, Tambutté E, de Beer D, Planas-Bielsa V, Tambutté S (2019) Full in vivo characterization of carbonate chemistry at the site of calcification in corals. Sci Adv 5:eaau7447

Sowa K, Watanabe T, Motai S, Seto Y, Nagai T (2008) Mineral phase of COCs and fibers in coral skeletons. In Proc. 11th Int. Coral Reef Symp 11:74–77

Stolarski J, Przeniosło R, Mazur M, Brunelli M (2007) High-resolution synchrotron radiation studies on natural and thermally annealed scleractinian coral biominerals. J Appl Crystallogr 40:2–9

Sun CY, Marcus MA, Frazier MJ, Giuffre AJ, Mass T, Gilbert PU (2017) Spherulitic growth of coral skeletons and synthetic aragonite: nature's three-dimensional printing. ACS Nano 11:6612–6622

Tambutté S, Holcomb M, Ferrier-Pagès C, Reynaud S, Tambutté E, Zoccola D, Allemand D (2011) Coral biomineralization: from the gene to the environment. J Exp Mar Biol Ecol 408:58–78

Toby BH, Von Dreele RB (2013) GSAS-II: the genesis of a modern open-source all purpose crystallography software package. J Appl Crystallogr 46:544–549

Van de Locht R, Verch A, Saunders M, Dissard D, Rixen T, Moya A, Kröger R (2013) Microstructural evolution and nanoscale crystallography in scleractinian coral spherulites. J Struct Biol 183:57–65

Venn A, Tambutté E, Holcomb M, Allemand D, Tambutté S (2011) Live tissue imaging shows reef corals elevate pH under their calcifying tissue relative to seawater. PloS One 6:e20013

Von Euw S, Zhang Q, Manichev V, Murali N, Gross J, Feldman LC, Gustafsson T, Flach C, Mendelsohn R, Falkowski PG (2017) Biological control of aragonite formation in stony corals. Science 356:933–938